Chem Soc Rev

# Atomistic simulation of transport phenomena in nanoelectronic devices



| | |
|---|---|
| Journal: | *Chemical Society Reviews* |
| Manuscript ID: | CS-TRV-02-2014-000084.R1 |
| Article Type: | Tutorial Review |
| Date Submitted by the Author: | 27-Mar-2014 |
| Complete List of Authors: | Luisier, Mathieu; ETH Zürich, |
| | |

ARTICLE TYPE www. rsc.org/xxxxxx | XXXXXXXX

# Atomistic simulation of transport phenomena in nanoelectronic devices

**Mathieu Luisier**[a]

***Received Xth XXXXXXXXXX 20XX, Accepted Xth XXXXXXXXX 20XX***
***First published on the web Xth XXXXXXXXXX 20XX***
**DOI: 10.1039/b000000x**

Computational chemistry deals with the first-principles calculation of electronic and crystal structures, phase diagrams, charge distributions, vibrational frequencies, or ion diffusivity in complex molecules and solids. Typically, none of these numerical experiments allows for the calculation of electrical currents under the influence of externally applied voltages. To address this issue, there is an imperative need for an advanced simulation approach capable of treating all kind of transport phenomena (electron, energy, momentum) at a quantum mechanical level. The goal of this tutorial review is to give an overview of the "quantum transport" (QT) research activity, introduce specific techniques such as the Non-equilibrium Green's Function (NEGF) formalism, describe their basic features, and underline their strengths and weaknesses. Three examples from the nanoelectronics field have been selected to illustrate the insight provided by quantum transport simulations. Details are also given about the numerical algorithms to solve the NEGF equations and about strategies to parallelize the workload on supercomputers.

## Key learning points

1. State-of-the-art in atomistic device modeling
2. Introduction to quantum transport techniques with an arbitrary orbital basis
3. Differences between closed, periodic, and open boundary conditions
4. Working principle of different nanoelectronic devices with emphasis on transistors
5. Utility of supercomputers in computational nanotechnology

## 1 Introduction

The functionality of nanoelectronic devices such as ultra-thin-body transistors[1], molecular switches[2], nanowire thermoelectric generators[3], quantum well solar cells[4], or quantum dot light emitting diodes[5] strongly depends on the materials they are made of. In fact, the concepts of "new materials" and "new devices" converge towards each other at the nanometer scale: modifying the dimensions of a given nanostructure directly affects its material properties (band gap, effective mass, quantized energy levels, absorption coefficient, electron/hole mobility, or thermal conductivity), while replacing a material by another one changes the size, shape, and composition requirements to achieve the targeted figures of merit (magnitude of the drive and leakage currents, absorption efficiency, or switching speed). As a consequence, fabricating nano-devices that properly work and fulfill the foreseen specifications is a very challenging task and a complicated, expensive, and time-consuming process. The first prototypes rarely achieve the desired characteristics and many fabrication cycles are necessary before a satisfactory level of performance can be obtained. For all these reasons, it clearly appears that designing nanoscale devices has become so tedious that it cannot be accomplished without the support of advanced simulation tools offering a materials science and device perspective.

Ab-initio (from first-principle) software packages such as VASP[6], ABINIT[7], Quantum ESPRESSO[8], SIESTA[9], or CP2K[10] are widely recognized as essential tools to shed light on the material properties of nanostructures like their electronic structures, phase diagrams, molecular dynamics, charge distributions, or crystal vibrations. For that purpose, they implement density-functional theory (DFT) methods based on the evaluation of the Kohn-Sham equations[11]. Although very

[a]*Integrated Systems Laboratory, ETH Zurich, Gloriastrasse 35, CH-8092 Zurich, Switzerland, Fax: +41 44 632 11 94; Tel: +41 44 632 53 33; E-mail: mluisier@iis.ee.ethz.ch*

powerful these full-band approaches have technical and conceptual limitations. One of them is their heavy computational burden and long calculation times. This prevents the consideration of large atomic systems and/or out-of-equilibrium transport situations where electrons move due to externally applied voltages and temperature differences. Hence, DFT calculations are usually limited to small-size structures in equilibrium with their environment and composed of less than 1,000 atoms. Another limitation relates to the fundamentals of the method: DFT is a ground state theory that does not accurately capture the physics of unoccupied electron states, leading to an underestimation of the band gap of most semiconductors. Currently, novel solutions are emerging to solve this problem and give more accurate band gap values [12].

From a device point of view the objective is to compute particle flows in structures driven out-of-equilibrium and extract their "current vs. voltage" or "dissipated power vs. temperature" characteristics. At the nanometer scale this is only possible with a quantum transport simulator that accounts for energy quantization, quantum mechanical tunneling, and geometrical confinement. The Non-equilibrium Greens Function (NEGF) formalism, simultaneously introduced by Kadanoff/Baym [13] and Keldysh [14] in the 1960's, meets all these criteria. Since the beginning of the 1990's it has slowly imposed itself in the device modeling community as one of the most efficient techniques to simulate transport phenomena at the nanoscale [15].

The inclusion of open boundary conditions that couple a device with its out-of-equilibrium environment makes quantum transport calculations computationally very intensive and not really compatible with an ab-initio full-band model such as DFT. This is already true in the ideal case where electrons move along ballistic trajectories. When interactions with surfaces, impurities, crystal vibrations (phonons), and other electrons are considered, the physical complexity and the computation costs further increase [16], almost excluding the possibility for first-principles quantum transport simulations in the presence of scattering. However, since full-band and quantization effects are critical at the nanoscale and cannot be neglected, DFT is very often replaced by empirical models that are less accurate, but computationally more efficient. Tight-binding (TB) [17] represents a good example, but it is nor perfect either. The problem with TB comes from its parameterization that is done for specific atomic configurations, bulk usually, that do not necessarily correspond to the actual situation, out-of-equilibrium nanostructures. Because of this shortcoming, empirical models may lead to uncertainties in the results and lack of predictability. At the same time, they do not underestimate the band gap of semiconductors and they enable the investigation of quantum transport in large-scale domains, both in the ballistic limit of transport and with scattering.

Here, the basics of quantum transport calculations will be reviewed, starting from the derivation of open boundary conditions in Section 2, the inclusion of different scattering mechanisms in Section 3, and the benefits of empirical models such as tight-binding in Section 4. Three typical examples in the field of nanoelectronics have been selected to illustrate the physical quantities that can be observed with a quantum transport solver: (i) a carbon nanotube, (ii) a silicon nanowire, and (iii) a GaSb-InAs broken gap heterostructure. All these structures are investigated in Section 5. A possible scheme to reduce the simulation time through a massive parallelization of the workload is presented in Section 6. Finally, the review is summarized and conclusions are drawn in Section 7.

## 2 From electronic structure to quantum transport calculations

Quantum transport theories do not only apply to electrons, but also to phonons or photons. This review will mainly focus on electron transport, but will also briefly treat phonons since they are needed to describe electron-phonon interactions. The starting point is the single-particle Schrödinger equation

$$\hat{H}\psi(r) = E\psi(r), \quad (1)$$

$$\hat{H} = -\frac{\hbar^2}{2m_0}\nabla^2 + \hat{V}_{eff}(r), \quad (2)$$

where $\hbar$ refers to the reduced Planck constant and $m_0$ to the rest electron mass. Many-body effects are cast into the effective potential $\hat{V}_{eff}(r)$. The wave function $\psi(r)$ is not directly computed, but expanded in a basis. While in electronic structure calculations any basis is possible, in quantum transport applications, it is more convenient to use a localized basis, as explained later. The wave function $\psi(r)$ becomes then

$$\psi(r) = \sum_{n,\sigma} c_n^\sigma \phi_\sigma(r - R_n) \quad (3)$$

with the unknown expansion coefficients $c_n^\sigma$ and the basis functions $\phi_\sigma(r-R_n)$ of type $\sigma$ and centered at position $R_n$. Typically, the $\phi_\sigma(r-R_n)$'s take the form of linear combinations of atomic orbitals [9], contracted Gaussian functions [10], Löwdin orbitals [17], or Wannier functions [18]. By plugging Eq. (3) into Eq. (1), left-multiplying it by a basis function, and integrating over space, the following matrix elements

$$H_{nm}^{\sigma_1\sigma_2} = \int \mathrm{d}r^3 \; \phi_{\sigma_1}^*(r-R_n)\hat{H}\phi_{\sigma_2}(r-R_m) \quad (4)$$

$$S_{nm}^{\sigma_1\sigma_2} = \int \mathrm{d}r^3 \; \phi_{\sigma_1}^*(r-R_n)\phi_{\sigma_2}(r-R_m) \quad (5)$$

arise between the atom positions $R_n$ and $R_m$ and orbitals $\sigma_1$ and $\sigma_2$. They must be carefully evaluated in order to solve the Schrödinger equation. What differentiates density-functional theory (DFT) from empirical tight-binding or

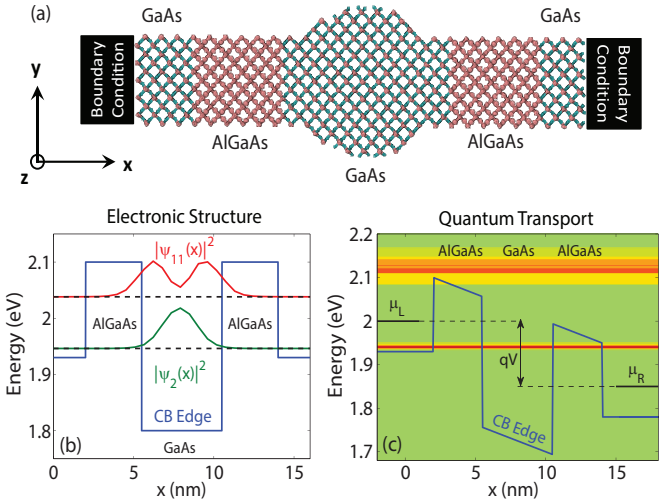


**Fig. 1** (a) Schematic view of a GaAs quantum dot embedded between two AlGaAs barriers and GaAs extensions. Depending on the choice of the boundary conditions (black blocks), either (b) electronic structure or (c) quantum transport calculations are performed. In (b), the second $|\psi_2(x)|^2$ and the eleventh $|\psi_{11}(x)|^2$ electron state of the nanostructure are plotted together with the conduction band diagram (periodic boundary conditions). Subplot (c) shows the spectral current (current as a function of the transport axis $x$ and electron energy $E$) flowing through the device in (a) when a voltage difference $V$ is applied (open boundary conditions). Red indicates high current concentrations, green no current. The difference between the chemical potential (Fermi levels) of the left $\mu_L$ and right $\mu_R$ contact is equal to $qV$.

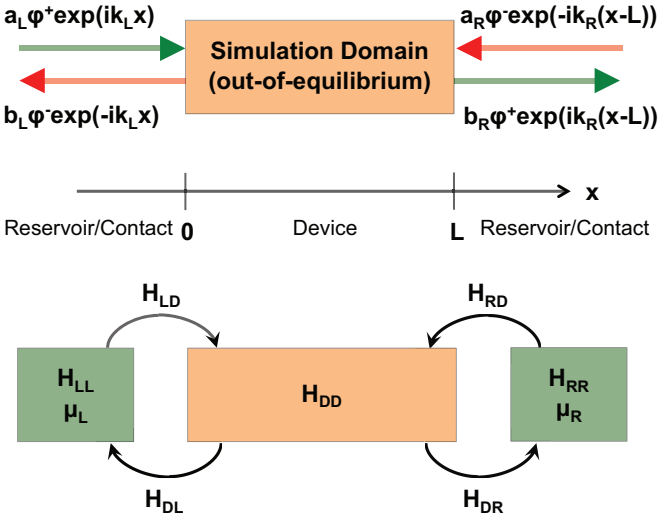


**Fig. 2** (a) Illustration of the open boundary condition mechanism in a two-terminal device. Plane waves are injected into the simulation domain from a left and right reservoir/contact with a probability $a_L$ and $a_R$, respectively. These coefficients are proportional to the electron distribution in the contact regions, which in turn depends on the chemical potentials $\mu_L$ and $\mu_R$. The $b$'s refer to the out-going waves, either reflected or transmitted. (b) Hamiltonian matrices representing the device ($\mathbf{H_{DD}}$), the left reservoir ($\mathbf{H_{LL}}$), the right one ($\mathbf{H_{RR}}$) as well as the coupling between the reservoirs and the device ($\mathbf{H_{LD}}$, $\mathbf{H_{DL}}$, $\mathbf{H_{RD}}$, and $\mathbf{H_{DR}}$).

pseudo-potential methods are the approximations that are made to Eqs. (4) and (5), as discussed in Section 4.

The boundary conditions (BCs) represent a critical aspect of Eq. (1). In electronic structure calculations, the most popular approaches are closed (hard wall potential) and periodic (repetition of the same structure) BCs. In the first case (closed), the wave function $\psi(r)$ is set to 0 at the boundaries (Dirichlet BCs), in the second case, the probability $|\psi(r)|^2$ is continuous at the interface between the simulation domain and its image, i.e. in a one-dimensional structure of length $L$ with $0 \leq x \leq L$, $|\psi(L)|^2 = |\psi(0)|^2$ and $\psi(L) = \exp(i\varphi)\psi(0)$.

Neither closed nor periodic boundary conditions lend themselves to quantum transport calculations. Electrons need to be able to enter and leave the simulated region with any probability between 0 and 1. In a two-terminal device with a left and right reservoir/contact, no injection can happen if the wave function is equal to 0 at the boundaries. With periodic BCs, the electrical properties of the two contacts must be identical, which does not allow for the application of an external voltage. Quantum transport requires open boundary conditions (OBCs) that are illustrated in Fig. 1 for a GaAs quantum dot embedded between two AlGaAs barriers and two GaAs reservoirs. With closed boundary conditions, discrete and confined states arise in the central quantum dot. Two examples are shown in Fig. 1(b). With OBCs, these states get broadened and form conduction channels for the electrons, as seen around the energy $E$=1.94 eV in Fig. 1(c). The key feature of the OBCs resides in the total separation of the left and right contact properties. They can have different geometries, electrostatic potential, or Fermi levels. Note that OBCs are not restricted to two contacts, but can be generalized to $N$ ports of entry [19].

The tricks to introduce OBCs in the Schrödinger equation are presented in Fig. 2. First, the contacts are assumed to be semi-infinite regions divided into unit cells defined in such a way that atomic connections exist only between adjacent cells. Then, all these unit cells have identical properties, both in term of their atomic configuration and in term of their electrostatic potential. Hence, the propagation of electrons along the injection direction can be modeled with a plane wave. This approach is known as quantum transmitting boundary method [20].

After some algebra, the Schrödinger equation with open boundary conditions can be written as [21]

$$\left(E \cdot \mathbf{S_{DD}} - \mathbf{H_{DD}} - \Sigma^B(E)\right) \cdot \mathbf{c}(E) \quad = \quad \mathbf{Inj}(E). \qquad (6)$$

In this Wave Function (WF) approach, the matrix $\mathbf{H_{DD}}$ ($\mathbf{S_{DD}}$) contains all the elements $H_{nm}^{\sigma_1\sigma_2}$ ($S_{nm}^{\sigma_1\sigma_2}$) between two

atoms/orbitals situated at positions $R_n$ and $R_m$. It is very sparse because most of its entries are equal to 0 (no atomic connection). In applications with a unique transport direction, $\mathbf{H_{DD}}$ and $\mathbf{S_{DD}}$ show a block-tri-diagonal structure that can be leveraged by dedicated numerical algorithms to solve quantum transport problems more efficiently[19].

All the expansion coefficients $c_n^\sigma$ become energy-dependent and are squeezed into the $\mathbf{c}(E)$ vector. It is important to realize that $\mathbf{c}(E)$ has multiple columns, some of them corresponding to states injected from the left contact, some of them from the right contact, all being independent from each other. Not shown in Eq. (6) is the momentum- or $k$-dependence, i.e. $\mathbf{c}(E)$ is in fact $\mathbf{c}(E,k)$. It only occurs in structures with periodicity along at least one of its transverse directions and is omitted here for brevity. The OBCS are cast into the self-energy matrix $\Sigma^B(E)$ and the injection vector $\mathbf{Inj}(E)$. Both quantities depend on the matrices $\mathbf{H_{LD}}$, $\mathbf{H_{DL}}$, $\mathbf{H_{RD}}$, and $\mathbf{H_{DR}}$ that connect the simulation domain with its contacts. In $\Sigma^B(E)$ only the entries that correspond to atoms with direct connections to the contact regions differ from 0. They are located in the upper left and lower right corner of the $\Sigma^B(E)$ matrix. This sparsity pattern comes from the usage of a localized basis set.

The size of the linear system of equations in Eq. (6) is $N_A \times N_{orb}$, where $N_A$ is the number of atoms in the device and $N_{orb}$ the number of orbitals per atom. Equation (6) must be solved for each electron energy $E$ and momentum $k$ before the $\mathbf{c}$ coefficient are summed up to give the charge density $\rho(r)$ and current $I_d$ flowing through the considered structures[21]. The charge $\rho(r)$ induces an electrostatic potential $V(r)$ that is calculated with the Poisson equation and inserted in the Hamiltonian operator $\hat{H}$ in Eq. (1). Hence, the Schrödinger and Poisson equations are self-consistently coupled and must be solved iteratively until convergence is achieved.

A retarded Green's function $\mathbf{G^R}(E)$ can be computed from Eq. (6) instead of the vector $\mathbf{c}(E)$. They are related through

$$\left(E \cdot \mathbf{S_{DD}} - \mathbf{H_{DD}} - \Sigma^B(E)\right) \cdot \mathbf{G^R}(E) = \mathbf{I} \tag{7}$$

$$\mathbf{c}(E) = \mathbf{G^R}(E) \cdot \mathbf{Inj}(E) \tag{8}$$

where $\mathbf{I}$ is the identity matrix. This is the so-called Non-equilibrium Green's Function (NEGF) formalism for quantum transport problems. One of the strength of NEGF comes from its ability to compute $\rho(r)$ and $I_d$ without evaluating $\mathbf{c}(E)$ as an intermediate step[15]. In ballistic transport simulations, all the observables can be derived from $\mathbf{G^R}(E)$, especially the transmission probability $T(E)$ between two contacts. The current $I_d$ is then calculated with the Landauer formula[22]

$$I_d = -\frac{e}{\hbar}\int \frac{dE}{2\pi} T(E)\left(f(E,E_{fL}) - f(E,E_{fR})\right) \tag{9}$$

with the elementary charge $e$. Here, it is assumed that the electrons move between two contacts (left and right) characterized by the Fermi level $E_{fL}$ and $E_{fR}$, respectively.

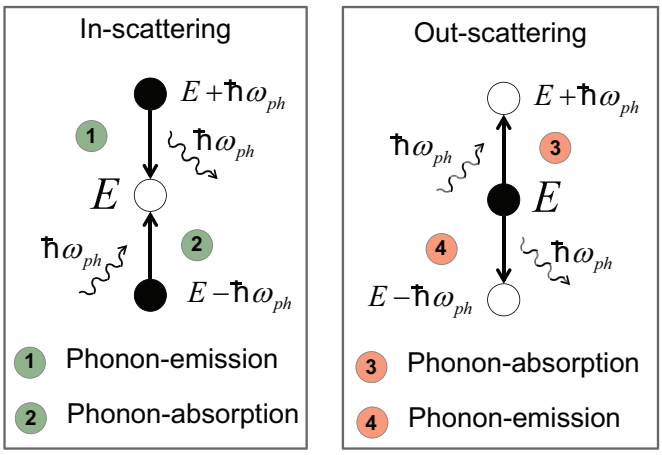


**Fig. 3** In- and out-scattering probability for an electron with energy $E$ interacting with a phonon with frequency $\omega_{ph}$. Through phonon emission or absorption, an empty state can be filled (in-scattering) or an occupied state can be emptied (out-scattering).

## 3 Beyond ballistic transport

Additional Green's Functions are required in the presence of scattering such as electron-phonon or anharmonic phonon-phonon interactions. Apart from the retarded $\mathbf{G^R}(E)$ Green's function, a lesser $\mathbf{G^<}(E)$ and greater $\mathbf{G^>}(E)$ component must also be taken into account in the NEGF formalism. The matrix entries $G_{nm}^{<\sigma 1\sigma 2}(E)$ and $G_{nm}^{>\sigma 1\sigma 2}(E)$ describe the correlations between the orbital $\sigma_1$ at position $R_n$ and $\sigma_2$ at $R_m$ and if $n$=$m$, the probability that a state is occupied ($<$) or unoccupied ($>$). The origin of the different Green's Functions and the derivation of their time-dependent equations of motion can be found in Ref.[23] and references therein.

In stationary quantum transport simulations, the time arguments are Fourier-transformed, giving rise to an energy dependence of all the Green's Functions[24]. For electrons, the following system of equations must be solved

$$\begin{cases} \left(E \cdot \mathbf{S}_{DD} - \mathbf{H_{DD}} - \Sigma^{RB}(E) - \Sigma^{RS}(E)\right) \cdot \mathbf{G^R}(E) = \mathbf{I} \\ \mathbf{G}^{\gtrless}(E) = \mathbf{G^R}(E) \cdot \left(\Sigma^{\gtrless B}(E) + \Sigma^{\gtrless S}(E)\right) \cdot \mathbf{G^A}(E). \end{cases} \tag{10}$$

In Eq. (10), the advanced Green's Function $\mathbf{G^A}(E)$ is equal to $(\mathbf{G^R}(E))^\dagger$. Furthermore, lesser and greater self-energies $\Sigma^{\gtrless}$ are introduced. They indicate the probability for in-scattering ($<$, an unoccupied state gets filled) and out-scattering ($>$, an occupied state becomes empty). All the self-energies can be of boundary (index $B$) or scattering (index $S$) type. The latters are used to model the desired scattering mechanisms, for example

| Structure | Model | $N_A$ | $N_{CPU}$ | OBCs (s) | LSEs (s) | Total Time (s) | Factor |
|---|---|---|---|---|---|---|---|
| CNT $d$=0.6 nm | TB | 2560 | 1 | 1.4e-3 | 4.72e-2 | 4.86e-2 | - |
| CNT $d$=0.6 nm | DFT | 2560 | 8 | 25.7 | 13.5 | 39.2 | 6600x |
| NW $d$=2.2 nm | TB | 10560 | 1 | 1.7 | 12.2 | 13.9 | - |
| NW $d$=2.2 nm | DFT | 10560 | 64 | 213 | 236 | 449 | 2070x |
| NW $d$=2.5 nm | TB | 12096 | 1 | 4.6 | 28.9 | 33.5 | - |
| NW $d$=2.5 nm | DFT | 12096 | 64 | 353 | 415 | 768 | 1470x |

**Table 1** Time to solve the Schrödinger equation with open-boundary conditions in a carbon nanotube with a diameter $d$=0.6 nm, in a Si nanowire with $d$=2.2 nm, and in another Si nanowire with $d$=2.5 nm. All the structures are 35 nm long. As basis in Eq. (3) tight-binding (TB) and density-functional theory (DFT) with Gaussian functions have been selected. The number of atoms in the structure ($N_A$), the number of CPUs used for the calculation ($N_{CPU}$), the time to compute the open boundary conditions, the time to solve Eq. (6), the total time, and the DFT/TB time ratio multiplied by $N_{CPU,DFT}$ are reported. All the numerical experiments have been performed on a Cray-XE6 machine.

electron-phonon interactions[25]

$$\Sigma^{\gtrless S}(E) = i\hbar \int \frac{d\omega}{2\pi} |M_{e-ph}|^2 \left( G^{\gtrless}(E-\hbar\omega)D^{\gtrless}(\omega) + G^{\gtrless}(E+\hbar\omega)D^{\lessgtr}(\omega) \right). \quad (11)$$

Here, $M_{e-ph}$ describes the strength of the electron-phonon coupling and the $D^{\gtrless}(\omega)$'s are the greater/lesser phonon Green's Functions at frequency $\omega$, where the lesser (greater) component gives the number of occupied (unoccupied) phonon states at $\omega$. The retarded scattering self-energy $\Sigma^{RS}(E)$ are derived from the value of $\Sigma^{\gtrless S}(E)$[16].

A visual interpretation of Eq. (11) can be found in Fig. 3. In the in-scattering case ($\Sigma^{<S}$, left subplot), an unoccupied state at energy $E$ is filled through the absorption by a filled state situated at $E-\hbar\omega$ ($G^{<}(E-\hbar\omega)$) of a phonon with frequency $\omega$ ($D^{<}(\omega)$). A similar in-scattering process occurs if a filled state at energy $E+\hbar\omega$ ($G^{<}(E+\hbar\omega)$) emits a phonon with frequency $\omega$. This requires the availability of phonon states at this frequency, which depends on $D^{>}(\omega)$. With the same arguments, the out-scattering processes can be explained.

The phonon Green's Functions can be calculated in different ways. The most simple one consists in assuming that the phonon population is at equilibrium so that the $D^{\gtrless}(\omega)$'s are approximated by Bose-Einstein distribution functions[26]. In the case of an out-of-equilibrium phonon population, a dynamical equation with open boundary conditions must be solved. It has the same form as Eq. (10), but the Hamiltonian matrix $\mathbf{H_{DD}}$ is replaced by a dynamical matrix $\Phi_{DD}$, the electron energy $E$ by $\omega^2$, and the self-energies are labeled $\Pi^{R,\gtrless}(\omega)$ instead of $\Sigma^{R,\gtrless}(E)$[27]. As for the Hamiltonian matrix, $\Phi_{DD}$ can be evaluated at the ab-initio or empirical level, the pendant of tight-binding for phonons being the valence-force-field model with a Keating potential[28].

A critical issue in quantum transport simulations with scattering is the coupling of Eqs. (10) and (11). The Green's Function equations depend on the scattering self-energies, which in turn exhibit a Green's Function dependence. Hence, both equations must be solved self-consistently till convergence. From 10 to 100 iterations might be necessary to reach this point, depending on the material, structure, and bias conditions. This is a computationally very intensive process that cannot be avoided. Non-self-consistent schemes have recently started to emerge[29], but their accuracy still needs to be carefully assessed in realistic devices.

In the presence of dissipative scattering, the current $I_d$ cannot be computed as in Eq. (9) any more because no transmission function $T(E)$ can be defined. In this case, it is evaluated at each position $x_n$ along the transport direction as[30]

$$I_d(x_n) = \frac{e}{\hbar} \sum_{i\in x_n} \sum_{j\in x_{n+1}} \int \frac{dE}{2\pi} \mathrm{tr}\left( H_{ij}G^{<}_{ji}(E) - G^{<}_{ij}(E)H_{ji} \right), \quad (12)$$

where $G^{<}_{ij}$ and $H_{ij}$ are blocks of size $N_{orb}\times N_{orb}$, tr indicates the trace operator, and the index $i$ ($j$) refers to atoms situated in the plane with $x$=$x_n$ ($x$=$x_{n+1}$). Equation (12) calculates the net transfer of electrons from the plane $x$=$x_n$ to $x$=$x_{n+1}$, which corresponds to the current flow at this location. After convergence of the iterative process between Eqs. (10) and (11), the current $I_d$ should be conserved, i.e. the values $I_d(x_n)$ must be the same for all the $x_n$'s. It can be demonstrated that in the ballistic limit of transport, Eq. (12) can be rearranged and then becomes identical to Eq. (9)[30].

## 4 The need for empirical models

As explained in the previous Section, the time-to-solution in quantum transport simulation might be really large, even in the ballistic limit of transport. It is therefore a goal of utmost importance to reduce the simulation time through algorithmic improvements or proper physical simplifications. The shape of the $H^{\sigma_1\sigma_2}_{nm}$ and $S^{\sigma_1\sigma_2}_{nm}$ matrix elements in Eqs. (4) and (5) is a major factor to accelerate the calculation of the open boundary conditions and the solution of the Schrödinger equation.

In a first-principles approach, the Hamiltonian operator $\hat{H}$ contains a kinetic term and an effective potential that varies rapidly in space. Pseudo-potentials eliminating the influence of the very localized core electrons and mimicking the true potential can be used to smooth these variations [31]. Still, the space integral in Eq. (4) must be computed on a very fine grid, which is a time-consuming operation.

A more serious issue stems from the long-range extension of the basis functions in Eq. (4). Contracted Gaussian functions, as utilized in the CP2K tool, can be delocalized over several nanometers and connect atoms that are far away. The same happens with linear combination of atomic orbitals so that it is not uncommon to deal with connections between seventh-nearest neighbor atoms or more. As a consequence, the sparsity of the Hamiltonian matrix $\mathbf{H_{DD}}$ in Eq. (6) rapidly decreases while the computational burden induced by the calculation of the open-boundary conditions and the Schrödinger equation drastically increases. Despite all these challenges, the first ab-initio quantum transport simulator was demonstrated more than a decade ago [32].

Empirical tight-binding models enable a faster evaluation of Eq. (4) by approximating it as the multiplication of a form factor that depends on the vector $R_n - R_m$ connecting the two neighbor atoms and of a material-specific constant [17]

$$H_{nm}^{\sigma_1\sigma_2} = \sum_b f_b^{\sigma_1\sigma_2}(R_n - R_m) \times V_{\sigma_1\sigma_2,b} \qquad (13)$$

In Eq. (13), the form factors $f_b^{\sigma_1\sigma_2}(R_n - R_m)$ and the material parameters $V_{\sigma_1\sigma_2,b}$ are different for each bond configuration $b$ that can be of $\sigma$-, $\pi$-, or $\delta$-type. While the $f_b^{\sigma_1\sigma_2}(R_n - R_m)$'s are derived from geometrical considerations and the properties of spherical harmonics, the $V_{\sigma_1\sigma_2,b}$'s are not directly computed, but used as fitting parameters so that the bandstructure of the investigated crystals is accurately reproduced around the points of high symmetry in the Brillouin Zone. In an orthogonal $sp^3d^5s^*$ basis with 20 orbitals per atom, nearest-neighbor connections are sufficient to model most semiconductors [33]. It results very sparse $\mathbf{H_{DD}}$ and diagonal $\mathbf{S_{DD}}$ matrices in Eq. (6).

The benefit of tight-binding in terms of computational efficiency can be observed in Table 1: the time to solve Eq. (6) with a tight-binding and DFT basis is reported for a carbon nanotube, and two silicon nanowires. Only one single energy point is computed. It turns out that DFT quantum transport calculations are about three orders of magnitude more expensive than tight-binding ones, thus severely limiting the size of the structures that can be studied at the ab-initio level. They further require the usage of massively parallel algorithms, especially for the evaluation of the open boundary conditions [34]. Note that if Eq. (7) (NEGF) is solved instead of Eq. (6) (WF), the computational intensity is at least one order of magnitude larger, both with a tight-binding and DFT basis. Also, the parallelization of the WF formalism is more straightforward than that of NEGF [35]. These facts, combined with the mandatory Green's Function / self-energy iterations in the presence of scattering, explain why quantum transport simulations are mostly restricted to the ideal ballistic case.

## 5 Applications

### 5.1 Short transistor review

Three nano-device applications have been chosen to illustrate the quantum transport methodology presented in this paper, (i) a carbon nanotube, (ii) a silicon nanowire, and (iii) a GaSb-InAs broken gap heterostructure. All operate as transistors, i.e. as binary switches, the active components of integrated circuits (ICs). After more than 40 years of aggressive scaling according to Moore's law [36], the size of the transistors does not exceed a few nanometers any more and their behavior is largely dominated by quantum mechanical effects.

The three structures proposed here represent possible evolutions of the transistor in an horizon of 5 to 10 years from now. They are all composed of a heavily doped source and drain extensions that are separated from each other by a potential barrier whose height is controlled by a gate contact. The latter is isolated from the semiconducting channel by a dielectric layer that minimizes leakage currents. Usually, the source contact is grounded while a voltage is applied to the drain and/or gate contact. This voltage may vary between 0 and $V_{DD}$, the transistor supply voltage. When $V_{gs}$, the gate-to-source voltage, is equal to 0 and $V_{ds}$, the drain-to-source voltage, to $V_{DD}$, the transistor is said to be in its OFF-state. When $V_{gs}$ and $V_{ds}$ are equal to $V_{DD}$, the ON-state is reached.

In a $n$-type ($p$-type) metal-oxide-semiconductor field-effect transistor (MOSFET), high-energy electrons (holes) overcome the gate-induced potential barrier that separates the source and drain. Because of the thermionic nature of this process, $V_{gs}$ must be changed by at least 60 mV to increase the electron/hole current by one order of magnitude. This "60 mV/dec" limit does not depend on the material or the number of gates. It is a serious obstacle to reduce the power consumption of ICs while keeping good characteristics. In effect, at a given $V_{DD}$, either a low OFF-current or a high ON-current is possible, but not both simultaneously.

In the sub-threshold regime of MOSFETs, at low $V_{gs}$ and $I_d$, electrons with an energy smaller than the potential barrier controlled by the gate, are reflected back to their origin, except if the channel length is short enough that quantum mechanical tunneling occurs. This phenomenon known as source-to-drain tunneling deteriorates the transistor performance and should be avoided at any costs. In band-to-band tunneling transistors (TFETS), this is exactly the opposite that is expected. The tunneling current should be maximized because it does not suffer from the 60 mV/dec limit [37], as detailed in Section 5.4.

### 5.2 Carbon nanotube

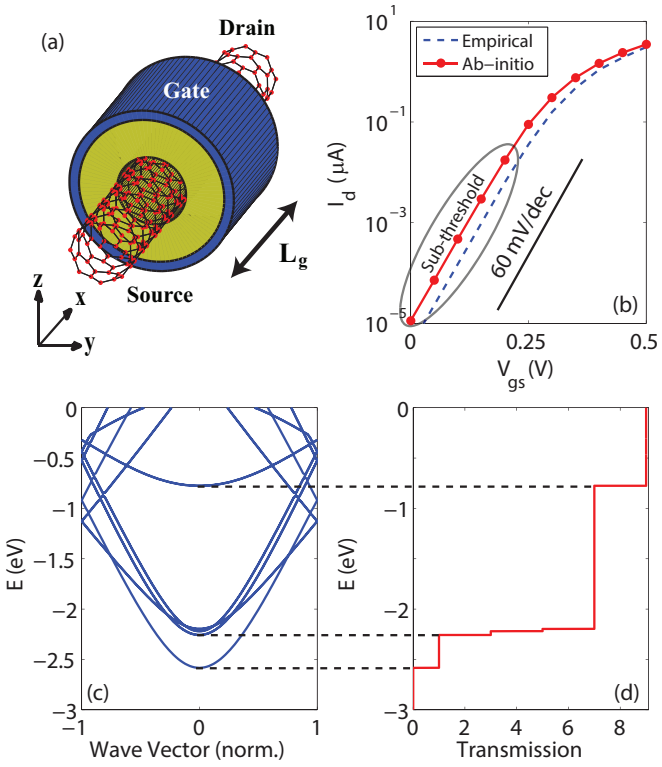


**Fig. 4** (a) Schematic view of a carbon nanotube field-effect transistor (CNTFET) composed of a source, drain, and gate region of length $L_g$. Electrons flow along the $x$-axis. The carbon atoms are depicted as red dots. (b) Transfer characteristics $I_d$-$V_{gs}$, i.e. current at the drain side as a function of the gate-to-source voltage, of a CNTFET with a diameter $d$=0.6 nm and $L_g$=15 nm. The drain-to-source voltage $V_{ds}$ is set to 0.5 V. The structure contains 2,560 atoms. Both an empirical (dashed line) and an ab-initio (solid line with circles) models have been used to compute $I_d$. (c) Conduction bandstructure of the same nanotube as in (b) calculated with an ab-initio model. (d) Energy-resolved transmission probability through the same structure as before. Each electron channel directly relates to the turn-on of a conduction sub-band.

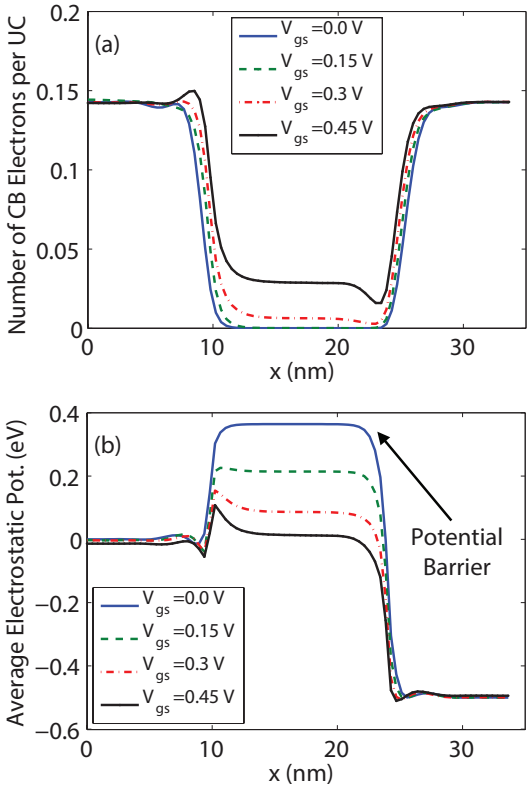


**Fig. 5** (a) Number of electrons in each unit cell of the CNTFET shown in Fig. 4 at different $V_{gs}$ and $V_{ds}$=0.5 V. (b) Average electrostatic potential energy as a function of $x$ and $V_{gs}$ for the same CNTFET as before. All the results have been obtained using an ab-initio representation of the simulation domain.

The first application is dedicated to a carbon nanotube field-effect transistor (CNTFET) as depicted in Fig. 4(a). The structure has a diameter of 0.6 nm, a gate length of 15 nm, and source and drain extensions of 10 nm each. This is exactly the same size as in Table 1. The first quasi-ballistic CNTFET was demonstrated in 2003[38]. Since then, a lot of progresses have been realized, placing this device architecture as a promising alternative to Si transistors.

Due to the low dimensions of the considered CNTFET, a quantum transport approach is necessary to simulate its current characteristics. With a total number of $N_A$=2,560 atoms only, both tight-binding (single $p_z$-orbital model with a hopping parameter $t_0$=-3 eV) and density-functional theory (3SP contracted Gaussian basis[10]) calculations can be done, as summarized in the $I_d - V_{gs}$ "current vs. gate voltage" subplot in Fig. 4. The DFT-TB comparison is made at the same potential barrier height between the source and drain extensions. It can be seen that the DFT current is larger than the TB one, especially at low voltages, and the inverse sub-threshold slope $iSS$=$\delta V_{gs}/\delta \log_{10}(I_d)$ is close to 60 mV/dec, the ideal value, in both cases. This indicates the absence of source-to-drain tunneling. The DFT underestimation of the CNT band gap ($E_{g,DFT}$=0.771 eV vs. $E_{g,TB}$=1.408 eV) is therefore not the reason for the current discrepancy. A more careful inspection of the DFT and TB results show that the bandstructures are different, leading to a higher DFT Fermi level and more current at the same barrier height.

The DFT conduction bandstructure of the carbon nanotube is shown in Fig. (4)(c) and the energy-resolved transmission probability from source to drain, assuming a flat potential, in subplot (d). Without any external perturbation the bandstructure and the transmission function are related to each other:

starting from a low energy and ramping it up, each time an additional sub-band with a positive velocity ($dE/dk > 0$) appears, a transmission channel turns on. For example, at an energy $E$=-1.5 eV, there are 7 bands available for transport and the transmission $T(E)$=7. In other words, the $T(E)$ simply counts the number of bands at a given energy $E$[39].

Quantum transport calculations also offers a deep insight into the electron distribution inside the CNTFET as well as the resulting electrostatic potential. Because the Schrödinger and Poisson equations are solved self-consistently, these two quantities strongly depend on each other. They are plotted in Fig. 5 for different gate-to-source voltages $V_{gs}$ at $V_{ds}$=0.5 V. To facilitate their visualization, the charge density and the electrostatic potential are averaged over the CNT cross section. As expected, when $V_{gs}$ increases, the height of the potential barrier between the source and the drain decreases, inducing more and more mobile electrons in the channel. When the free carrier density becomes large, it starts to screen the influence of the gate contact so that the barrier decrease between $V_{gs}$=0.3 and 0.45 V is much smaller than between $V_{gs}$=0 and 0.15 V when the channel was empty. Note finally that the electron concentration remains almost constant in the source and drain extensions where it must compensate the background doping. The channel region is assumed intrinsic.

### 5.3 Silicon nanowire

Silicon nanowires with diameters well below 10 nm have already been fabricated and wrapped by gate-all-around contacts to form ultra-scaled field effect transistors[40]. In these devices, electron transport can only be modeled at a quantum mechanical level. This is what has been done for the Si nanowire structure shown in Fig. 6(a). The semiconductor channel is oriented along the <100> crystal axis, it has a diameter $d$ of 3 nm and a total length $L$ of 35 nm decomposed into two heavily doped source and drain regions and a 15 nm long gate contact. A 1 nm thick $SiO_2$ oxide layer isolates the channel from the gate contact. The material properties of the $N_A$=16,019 Si atoms forming the nanowire are expressed in a $sp^3d^5s^*$ tight-binding basis[41]. Phonons are also simulated here with the valence-force-field model of Ref.[42].

The electron and phonon bandstructures of the considered Si nanowire are plotted in Fig. 6(b-c). Due to the geometrical confinement, the electron band gap increases from $E_g$=1.13 eV in bulk to 1.62 eV in the nanowire and the six bulk phonon bands are folded back to constitute $3\times N_A$ sub-bands. Before investigating transport in nanostructures it has been verified that a tight-binding + valence-force-field combined approach can accurately reproduce the experimental electron and hole mobility of bulk Si[43] as well as its bulk lattice thermal conductivity[44]. This is demonstrated in Fig. 6(d-e).

The current that flows through the Si nanowire transistor

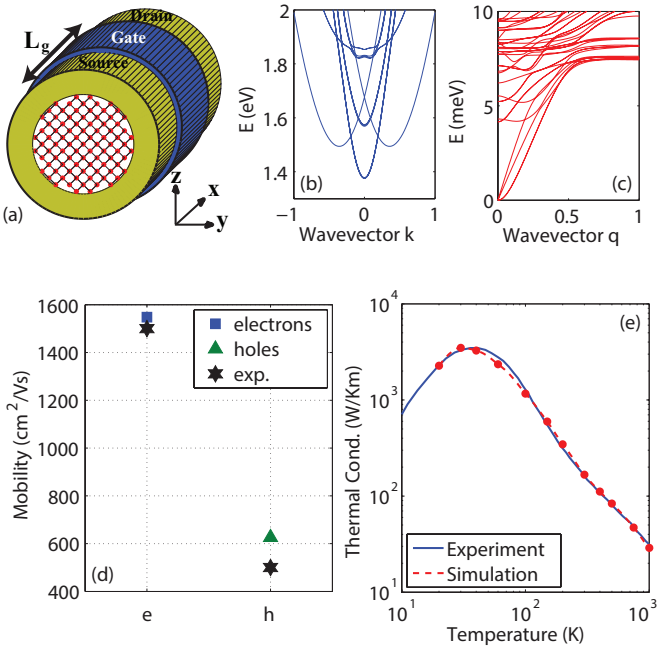


**Fig. 6** (a) Schematic view of a Si gate-all-around nanowire field-effect transistor (GAA NWFET). The red dots indicate Si atoms that form a semiconducting channel. It is surrounded by a dielectric material that isolates it from the gate contact. (b) Conduction bandstructure of a Si nanowire with a diameter $d$=3 nm as obtained with tight-binding. (c) Phonon bandstructure of the same nanowire as in (b) calculated with a valence-force-field (VFF) method. (d) Electron and hole mobility of bulk Si calculated from tight-binding in the presence of electron-phonon scattering. (e) Lattice thermal conductivity of bulk Si as a function of the external temperature as produced by VFF together with boundary and anharmonic phonon-phonon scattering.

of Fig. 6(a) is reported in Fig. 7 as a function of the gate-to-source voltage $V_{gs}$ at $V_{ds}$=0.6 V. Three cases have been studied: (i) ballistic transport, (ii) with electron-phonon scattering, and (iii) with self-heating effects. The difference between the second and third case comes from the phonon population. In (ii) it remains at equilibrium with the external environment so that the $D^{\gtrless}(\omega)$'s in Eq. (11) are replaced by Bose-Einstein distribution functions while in (iii) it is driven out-of-equilibrium and the phonon Green's Functions are explicitly solved. It results an energy transfer between the electron and phonon baths, locally increasing the lattice temperature (self-heating).

Irrespective of the transport model, the current increase in the sub-threshold region is limited to 60 mV/dec. When electron-phonon scattering is turned-on, the drain current drops by about 30% (equilibrium phonons) and by up to 50% (out-of-equilibrium), as compared to the ballistic limit. Backscattering explains this current reduction[45]. When electrons absorb or emit a phonon, they do not only undergo an

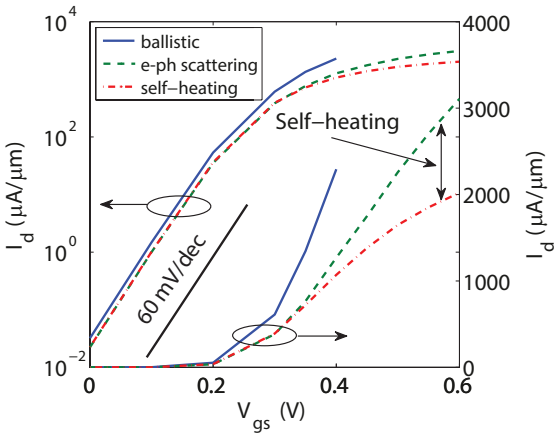


**Fig. 7** Transfer characteristics $I_d$-$V_{gs}$ at $V_{ds}$=0.6 V of a Si GAA NWFET with $d$=3 nm and $L_g$=15 nm. Solid line: in the ballistic limit of transport. Dashed line: with electron-phonon scattering, but an equilibrium phonon population. Dashed-dotted line: with both electrons and phonons driven out-of-equilibrium. Self-heating effects can be observed.

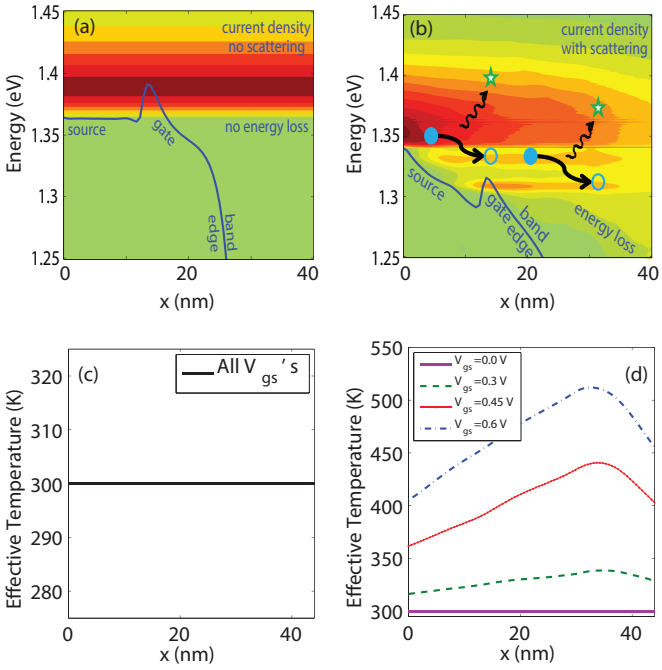


**Fig. 8** (a) Spectral current of the same GAA NWFET as in Fig. 7 in the ballistic limit of transport. (b) Same as (a), but with electron-phonon scattering. By emitting phonons (green stars) electrons (blue dots) loose energy while propagating from source to drain. (c) Spatially-resolved lattice temperature as a function of $V_{gs}$ extracted from the ballistic simulations and those with equilibrium phonons. Same as (c), but with self-heating. The lattice temperature increases with $V_{gs}$ and exhibits a maximum close to the drain region.

energy variation, but also a momentum one. If the latter becomes negative, the interacting electron is reflected back to its origin and the current magnitude decreases. Backscattering is especially important in the region before the top of the potential barrier. The increase of the phonon population caused by self-heating induces a higher probability for electrons to backscatter and therefore a lower drive current.

Figure 8 gives a different perspective on self-heating effects. In subplot (a) and (b), the spectral electron current is reproduced for the ballistic case and with electron-phonon scattering, respectively. Red indicates high current concentrations, green no current. It can be observed that without phonon interactions, the electrons keep the same energy from source to drain. In the presence of scattering, they loose energy through phonon emission so that the total electron energy on the drain side (right) is lower than on the source side (left). If it is assumed that the phonon population is at equilibrium, the energy lost by the electrons simply vanishes and the lattice temperature remains equal to the external one, 300 K, in the entire device structure, as in Fig. 8(c). In the out-of-equilibrium scenario, the lost energy is responsible for an increase of the lattice temperature, which is bias-dependent and more pronounced on the drain side[46], as shown in Fig. 8(d).

### 5.4 Broken gap heterostructure

Band-to-band tunneling (BTBT) transistors, also called TFETs, do not rely on thermionic currents as MOSFETs, but on the quantum mechanical tunneling of electrons from the valence band of a $p$-doped source region into the conduction band of a $n$-doped drain extension. Hence, cold instead of hot electrons compose the drive current, alleviating the 60 mV/dec limit of MOSFETs mentioned above[37]. If TFETs would work as expected, large ON-currents could be achieved at low OFF-currents and supply voltages. This is an essential condition to reduce the power consumption of integrated circuits. However, practically, no TFET satisfying all these requirements at the same time has been fabricated so far, mainly due to technological challenges.

An advanced quantum transport approach might help improve the design of TFETs, provided that it accurately models band-to-band tunneling currents. Due to its underestimation of band gaps, a DFT basis is not really suitable for that purpose, contrary to tight-binding, which fulfills the necessary criteria. To maximize the tunneling efficiency, a broken gap heterostructure, for example GaSb-InAs with GaSb in the source and InAs in the channel and drain, is advantageous. A region with no band gap exists between these two materials, at the source-channel interface, favoring band-to-band tunneling processes. Recently, GaSb-InAs Esaki (or BTBT) diodes have been successfully produced[47], but unlike transistors, they can-

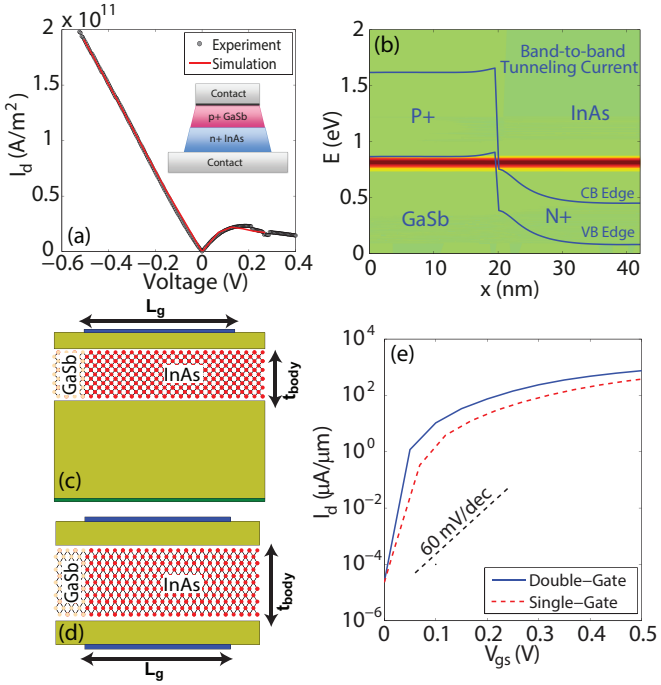


**Fig. 9** (a) Experimental[47] and simulated "current vs. voltage" characteristics of a GaSb-InAs broken gap Esaki diode. (b) Spectral current and band diagram of the diode in (a) at a voltage $V$=-0.2 V. (c) Schematic view of a single-gate ultra-thin-body GaSb-InAs band-to-band tunneling transistor (TFET) with a body thickness $t_{body}$=5 nm and gate length $L_g$=40 nm. (d) Same as (c), but for a double-gate structure. (e) Transfer characteristics $I_d$-$V_{gs}$ at $V_{ds}$=0.5 V of the two GaSb-InAs TFETs depicted in (c) and (d).

not operate as binary switches since they have only two contacts. Using a quantum transport simulator, their experimental current can be very well reproduced, as illustrated in Fig. 9(a). Subplot (b) shows that the current mainly flows through a band gap free energy window situated at the GaSb-InAs interface.

After verifying the accuracy of empirical tight-binding for GaSb-InAs heterostructures, the performance of band-to-band tunneling transistors made of the same material system can be reliably analyzed. A single-gate and double-gate ultra-thin-body, as schematized in Fig. 9(c-d), are simulated and their current characteristics reported in subplot (e). In both devices, the gate length measures $L_g$=40 nm and the channel thickness is set to $t_{body}$=5 nm. To avoid leakage currents, the doping concentration of the drain, $N_D$=5e18 cm$^{-3}$, is lower than that of the source, $N_A$=4e19 cm$^{-3}$. Two important features should be noticed from the simulation data: (i) the slope of the current at low voltage is well below the 60 mV/dec of MOSFETs, as expected from TFETs, and (ii) the double-gate transistor, due to a better electrostatic control, offers a higher ON-current at the same OFF-current[48]. These are theoretical results for ideal atomic arrangements. In reality, impurities at the GaSb-InAs interface and between the semiconductor channel and the insulator layers alter the transistor behavior so that low inverse sub-threshold slopes become extremely difficult to obtain[37]. At this point, there is still a lot of design and process optimization to do before TFETs can really challenge MOSFETs as future state-of-the-art binary switches.

## 6 Numerical aspects

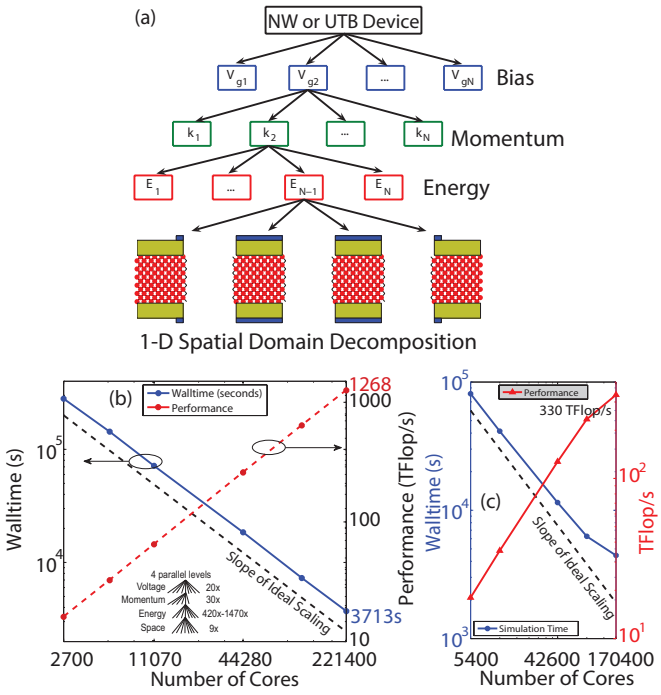


**Fig. 10** (a) Four-level parallelization scheme that can naturally be applied to quantum transport calculations: (i) bias points, (ii) momentum, (iii) energy, and (iv) 1-D spatial domain decomposition. (b) Illustration of the walltime strong scaling (blue line) and performance increase (red line) obtained by leveraging the parallel approach in (a) for the ballistic simulation of a realistic InAs transistor on 2,700 up to 221,400 cores. (c) Same as (b), but for a Si device including electron-phonon scattering. The number of cores ranges from 5,400 up to 170,400.

To reduce the computational costs of quantum transport calculations, the solution of the Schrödinger equation must be parallelized, i.e. Eqs. (6), (7), or (10) must be distributed over several central processing units (CPUs) that work in parallel to produce either expansion coefficients or Non-equilibrium Green's Functions. This spatial domain decomposition (each CPU stores only a fraction of the simulation domain) is the lowest possible parallelization level, but also the most difficult to realize. Since the Schrödinger equation must be solved

for each electron energy and momentum (only in structures with periodicity along at least one transverse direction), two additional levels of parallelism can be identified, the distribution of the energy and momentum points. Finally, at the highest level, each external voltage can be treated by a different group of CPUs, thus forming a fourth possibility of accelerating quantum transport simulations. A typical 4-level parallelization scheme including bias, momentum, energy, and spatial domain decomposition is shown in Fig. 10(a).

Inter-processor communication, if intensive, limits the parallel efficiency of a code or algorithm and should be avoided as much as possible. For example the distribution of the bias points is embarrassingly parallel, which means that each point can be handled independently from the others and no communication is needed. This is the ideal case. In ballistic transport simulations, the parallelization of the momentum and energy points has the same virtue because each Schrödinger equation is independent from the others. If electron-phonon interactions are turned on, the situation changes due to the calculation of the scattering self-energies, as in Eq. (11). The integral over the phonon frequency $\omega$ couples different energies (and momentum if present) together, making the implementation of dissipative transport simulations more complicated and reducing the parallel efficiency.

To demonstrate the acceleration potential brought by a massive parallelization of the computational tasks, two strong-scaling experiments are reported in Fig. 10, one dealing with ballistic transport in subplot (b) and one with dissipative transport in subplot (c). In both simulations, a two-dimensional transistor structure with a single-gate contact is investigated. A strong-scaling experiment consists in measuring the time needed to simulate a pre-defined device as a function of the number of CPUs, from 2,700 up to 221,400 in the ballistic case, from 5,400 up to 170,400 in the dissipative one. In subplot (b) the four levels of parallelism mentioned above are leveraged. The simulation time almost linearly decreases as the number of CPU increases. The parallel efficiency, defined as $t_{2,700}/t_{221,400}\times$2,700/221,400, exceeds 90% so that less than 1 hour is required on 221,400 cores to compute the "current vs. voltage" characteristics of the considered transistor instead of years on a single CPU[49]. In subplot (c), electron-phonon scattering reduces the parallel efficiency to about 70%. This is still more than acceptable for a real-world application, but poorer than without electron and momentum coupling. It is worthwhile noting that in this experiment only one single bias point has been computed. With ten bias points, a machine with more than 1 million CPUs could be very efficiently used.

Another important metrics in high performance computing (HPC) is the number of floating point operations per second (Flop/s) that is performed during a standard simulation. The ballistic run reached a sustained performance of 1.268 PFlop/s (1e15 Flop/s), which corresponds to 50% of the peak performance of the supercomputer that was used, a Cray-XT5. The sustained performance of the dissipative run drops to 20% due to the increased inter-processor communication. Still, typical applications operate at about 10% of the peak performance of supercomputers. Figure 10 shows that a well-implemented quantum transport simulator significantly outperforms this number[49].

## 7 Summary and Conclusion

The purpose of this tutorial review has been to give an overview of the quantum transport field and current research activities. The techniques to model electron, phonon, and/or photon flows through nanostructures have been introduced with a special emphasis on the inclusion of open boundary conditions and their differences with electronic structure calculations. To reduce the simulation time and allows for the consideration of diverse scattering mechanisms, it has been shown that an empirical basis such as tight-binding is preferred to first-principles approaches. Three applications, all dealing with nanoscale transistors, have been proposed as illustration of quantum transport simulations. Finally, the importance of parallel computing has been stressed out to accelerate ballistic and dissipative transport calculations.

As future challenges, quantum transport will have to evolve towards "ab-initio" modeling although the computational costs are much higher than with empirical methods. This direction seems to be the only one offering really predictive simulation capabilities that can be applied to any material configuration without the need for a sometimes complicated parameterization. The band gap problem of DFT approaches can be overcome by using hybrid functionals[12] and high performance computing can help minimize the computational burden. The highest hurdle will probably be the inclusion of scattering in a first-principles basis. There have been some attempts to reach this holly grail, but only in tiny atomic structures and without a fully self-consistent treatment of the Green's Function / scattering self-energy iterations[50]. The future availability of larger and larger supercomputers might help go one step further and enable ab-initio device simulators with dissipative quantum transport functionalities.

## 8 Acknowledgments

This work was supported by SNF grant PP00P2_133591, by the Hartmann Müller-Fonds on ETH Research Grant ETH-34 12-1, by a grant from the Swiss National Supercomputing Centre (CSCS) under project ID s363, by NSF grant EEC-0228390 that funds the Network for Computational Nanotechnology, by NSF PetaApps grant number 0749140, and by NSF

through XSEDE resources provided by the National Institute for Computational Sciences (NICS).

## References


1 B. S. Doyle, S. Datta, M. Doczy, S. Hareland, B. Jin, J. Kavalieros, T. Linton, A. Murthy, R. Rios, and R. Chau, *IEEE Elec. Dev. Lett.*, 2003, 24, 263.

2 C. Joachim, J. K. Gimzewski, and A. Aviram, *Nature*, 2000, 408, 541.

3 A. I. Hochbaum, R. Chen, R. D. Delgado, W. Liang, E. C. Garnett, M. Najarian, A. Majumdar, and P. Yang, *Nature*, 2008, 451, 163.

4 K. W. J. Barnham and G. Duggan, *J. App. Phys.*, 1990, 67, 3490.

5 P. O. Anikeeva, J. E. Halpert, M. G. Bawendi, and V. Bulovic, *Nano Lett.*, 2009, 9, 2532.

6 G. Kresse and J. Furthmüller, *Phys. Rev. B*, 1996, 54, 11169.

7 X. Gonze et al., *Comp. Phys. Commun.*, 2009, 180, 2582.

8 Paolo Giannozzi et al., *J. Physics: Condensed Matter*, 2009, 39, 395502.

9 J. Izquierdo, A. Vega, L. C. Balbás, D. Sánchez-Portal, J. Junquera, E. Artacho, J. M. Soler, and P. Ordejón, *Phys. Rev. B*, 2000, 61, 13639.

10 J. VandeVondele, M. Krack, F. Mohamed, M. Parrinello, T. Chassaing, and J. Hutter, *Comp. Phys. Comm.*, 2005, 167, 103.

11 W. Kohn and L. J. Sham, *Phys. Rev.*, 1965, 140, A1133.

12 A. V. Krukau, O. A. Vydrov, A. F. Izmaylov, and G. E. Scuseria, *J. Chem. Phys.*, 2006, 125, 224106.

13 L. Kadanoff and G. Baym, "Quantum Statistical Mechanics", Addison-Wesley Publishing (1962).

14 L. V. Keldysh, *ZhETF*, 1964, 47, 1515.

15 S. Datta, "Electronic Transport in Mesoscopic Systems", Cambridge University Press (1995).

16 R. Lake, G. Klimeck, R. C. Bowen, and D. Jovanovic, *J. Appl. Phys.*, 1997, 81, 7845.

17 J. C. Slater and G. F. Koster, *Phys. Rev.*, 1954, 94, 1498.

18 N. Marzari and D. Vanderbilt, *Phys. Rev. B*, 1997, 56, 12847.

19 A. Svizhenko, M. Anantram, T. Govindan, R. Biegel, and R. Venugopal, *J. Appl. Phys.*, 2002, 91, 2343.

20 C. S. Lent and D. J. Kirkner, *J. App. Phys.*, 1990, 67, 6353.

21 M. Luisier, and A. Schenk, *J. Comput. Theor. Nanosci.*, 2008, 5, 1031.

22 R. Landauer, *Philos. Mag.*, 1970, 21, 863.

23 P. Danielewicz, *Annals of Physics*, 1984 152, 239.

24 H. Haug and A.-P. Jauho, "Quantum Kinetics in Transport and Optics of Semiconductors", Springer (1996).

25 M. Luisier and G. Klimeck, *Phys. Rev. B*, 2009, 80, 155430.

26 G. D. Mahan, "Many-Particle Physics", Plenium (1990).

27 N. Mingo and L. Yang, *Phys. Rev. B*, 2003, 68, 245406.

28 P. Keating, *Phys. Rev.*, 1966, 145, 637.

29 H. Mera, M. Lannoo, C. Li, N. Cavassilas, M. Bescond, *Phys. Rev. B*, 2012, 86, 161404.

30 Y. Meir and N. S. Wingreen, *Phys. Rev. Lett.*, 1992, 68, 2512.

31 H. Hellmann, *J. Chem. Phys.*, 1935, 3, 61.

32 M. Brandbyge, J. L Mozos, P. Ordejon, J. Taylor, and K. Stokbro, *Phys. Rev. B*, 2002, 65, 165401.

33 J.-M. Jancu, R. Scholz, F. Beltram, and F. Bassani, *Phys. Rev. B*, 1998, 57, 6493.

34 E. Polizzi, *Phys. Rev. B*, 2009, 79, 115112.

35 M. Luisier, G. Klimeck, A. Schenk, and W. Fichtner, *Phys. Rev. B*, 2006, 74, 205323.

36 G. E. Moore, *Electronics*, 1965, 38, 114.

37 A. Ionescu and H. Riel, *Nature* 2011, 479, 329.

38 A. Javey, J. Guo, Q. Wang, M. Lundstrom, and H. Dai, *Nature*, 2003, 424, 654.

39 Y.-J. Ko, M. Shin, S. Lee, K. W. Park, *J. of Appl. Phys.*, 2001, 89, 374.

40 S. D. Suk et al., *IEDM Tech. Dig.*, 2005, 717-720.

41 T. B. Boykin, G. Klimeck, and F. Oyafuso, *Phys. Rev. B*, 2004, 69, 115201.

42 Z. Sui, I. P. Herman, *Phys. Rev. B*, 1993, 48, 17938.

43 Y.-M. Niquet, C. Delerue, D. Rideau, and B. Videau, *IEEE Trans. Elec. Dev.*, 2012, 59, 1480.

44 M. Luisier, *Phys. Rev. B*, 2012, 86, 245407.

45 M. S. Lundstrom, *IEEE Elec. Dev. Lett.*, 2001, 22, 293.

46 R. Rhyner and M. Luisier, *IEDM Tech. Dig.*, 2013, 32.1.1-32.1.4.

47 D. Pawlik et al., *IEDM Tech. Dig.*, 2012, 812-814.

48 M. Luisier and G. Klimeck, *IEDM Tech. Dig.*, 2009, 853-856.

49 M. Luisier, T. B. Boykin, W. Fichtner, and G. Klimeck, *Proc. of 2011 Int. Conf. for High Performance Computing, Networking, Storage and Analysis*, 2011, 2.1-2.11.

50 T. Frederiksen, M. Paulsson, M. Brandbyge, and A.-P. Jauho, *Phys. Rev. B*, 2007, 75, 205413.


 

Author picture
318x338mm (72 x 72 DPI)

**Mathieu Luisier** received his Ph.D. degree in 2007 from the ETH Zurich. He then joined the Network for Computational Nanotechnology, Purdue University, USA, as a research assistant professor before returning to the ETH in 2011 to become an assistant professor in computational nanoelectronics. His current research interests focus on the modeling of nanoscale devices such as nano-transistors, solar cells, or lithium-ion batteries. Mathieu Luisier was awarded the ETH medal for his diploma and Ph.D. thesis, he won an honorable mention at the ACM Gordon Bell Prize in 2011, and received an ERC Starting Grant in 2013.

Graphical abstract text:

This paper presents a sophisticated approach to treat quantum transport in nanostructures, covering the basic equations up to relevant applications.